



Universiteit  
Leiden  
The Netherlands

## Physics implications of shape on biological function

Pomp, W.

### Citation

Pomp, W. (2017, December 5). *Physics implications of shape on biological function*. *Casimir PhD Series*. Retrieved from <https://hdl.handle.net/1887/57789>

Version: Not Applicable (or Unknown)

License: [Licence agreement concerning inclusion of doctoral thesis in the Institutional Repository of the University of Leiden](#)

Downloaded from: <https://hdl.handle.net/1887/57789>

**Note:** To cite this publication please use the final published version (if applicable).

Cover Page



Universiteit Leiden



The handle <http://hdl.handle.net/1887/57789> holds various files of this Leiden University dissertation

**Author:** Pomp, Wim

**Title:** Physics implications of shape on biological function

**Date:** 2017-12-05

## Chapter 2

# Retention of neuronal receptors induced by spine-morphology<sup>†</sup>

Here we show that the morphology of the dendritic spine can be a significant determinant for regulating memory and learning. Using an artificial system that models the dendritic spine in a giant unilamellar vesicle, we experimentally confirmed the significance of spine-morphology on the escape of membrane-bound receptors from the spine, a process called 'the narrow escape problem'. Our results show that retention within the spine scales with spine-size beyond the predicted quadratic dependence reflecting the surface area. We show that the morphology of some dendritic spines can slow down the escape of receptors enough to give other biochemical processes a significant time-window to be set in motion. Furthermore, our analysis yields that the size of the spine-head determines receptor retention, rather than the length of the spine-neck.

---

<sup>†</sup>This chapter is based on: W. Pomp, R. P. T. Kusters, C. Storm and T. Schmidt "The narrow-escape problem revisited experimentally in an artificial system". *In preparation*.

## 2.1 Introduction

The brain is arguably the most complex organ in humans. It consists of almost 100 billion neurons which are interconnected by approximately 1000 connections each. Those connections, the synapses, are at the base of the brain's processing capabilities and its memory. Signals are transmitted between neurons by neurotransmitters which are released from the pre-synaptic neuron and detected by specialized transmembrane receptors on the post-synaptic neuron (figure 2.1). The processes of learning and memory are encoded by a change in the coupling strengths between synapses. This coupling strength is governed by the receptor density at the post-synaptic side. An increase in receptor density strengthens, while a decrease in receptor density weakens the coupling [1]. Hence, for memory, a constant receptor density in the synapse is required. One way to achieve a constant density would be to capture and immobilize all receptor molecules at the synapse. Yet, to a surprise, it was found, initially by fluorescence recovery after photobleaching experiments [2], and since firmly confirmed by single-molecule tracking [3–7] and superresolution microscopy [6], that receptors are mobile within the post-synaptic space, contradicting the earlier believe.

Simultaneously with the change in connection strength and receptor density, the postsynaptic neuron changes shape [8, 9]. Extensive studies using state-of-the-art electron microscopy [10] established a sequence of particular morphological changes at the location of the synaptic connection described by the formation of the so-called synaptic spine. With increasing coupling strength the spine changes morphology. From what is initially a small protrusion, it grows into a fully developed mushroom-shaped mature spine with a head typically a few tens of micrometers in diameter, being connected to the postsynaptic neuron through a very narrow membrane tube, or neck, of about ten to hundred nanometer diameter [11, 12]. Recently, the morphological change on learning has been followed directly in live cells [13] and in a live animal [14].

Those two observations have led to a unifying model for learning and memory that allows for the observed receptor mobility within the spine, which is required for short-term synaptic variability and likewise preventing swift loss of receptor density. The narrow neck slows down the escape of receptors from the dendritic spine, allowing other biochemical processes to kick in and ultimately keep the number of receptors in a dendritic spine at a constant level. One structure which is known to hinder the escape of receptors is the presence of a septin meshwork in the dendritic spine neck [15]. This model unites the seemingly mutually exclusive observations of receptor mobility and

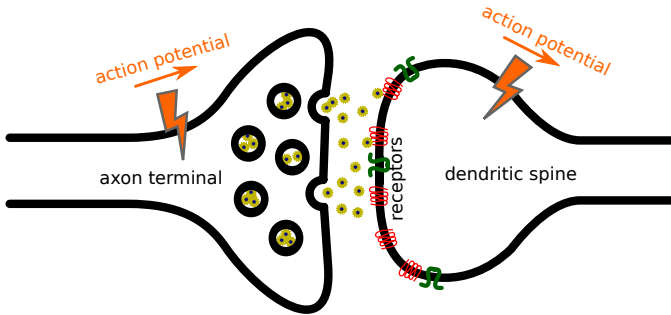


Figure 2.1: **The synapse.** Upon arrival of an action potential in the axon terminal, neurotransmitters are released into the synaptic cleft and are sensed by receptors in the membrane of the dendritic spine. In turn voltage channels are opened creating a new action potential in the dendrite.

receptor confinement. Theoretically, the geometric problem has been described in terms of the "narrow escape problem" [16]. Analytical studies [16], together with a recent simulation approach [17], have predicted that the change of morphology can, at least partially, explain how mobile receptors are restricted to the spine and thereby guarantee a stable strength of the synapse [18]. It is worth mentioning, that the narrow neck might also lead to a reduction in dimensionality for receptor diffusion, which can lead to unexpected behavior in biological processes [19]. Here, we set out for an experimental verification of the narrow-escape model.

## 2.2 Results

### 2.2.1 Mimetic system of the synaptic spine

We created an artificial system that mimics the mushroom-like morphology of the dendritic spine. This artificial system allowed us to set and vary the leading parameters defining the morphology in a large range, embracing those found in the brain. Our mimetic system consists of giant unilamellar vesicles (GUVs), from which membrane tubes were pulled. For the generation of GUVs, we used the process of electroswelling from pure phospholipids [20]. The size-range of GUVs was varied from 4 to 20  $\mu\text{m}$ . Such size-span of almost one order of magnitude has been reported for the heads of dendritic spines *in vivo* [12].

The spine neck we realized by pulling a membrane patch from the GUV by a fine pipette. Slight suction with simultaneous retraction of the pipette from the GUV using a micromanipulator allowed us to form a membrane tube of variable length. The resulting shape is depicted in figure 2.2 as a cross-section. It has been shown that the radius  $r$  of the tube depends on the square root of the ratio of the bending modulus and the surface tension of the membrane [21]. Whereas the bending modulus is a characteristic of the phospholipids used, the tension is determined by the method by which the GUVs were produced. The latter varied for each of our preparations. Hence the tube radius was determined experimentally in each experiment. It varied in a narrow window centered at 200 nm (Supplementary figure 2.10).

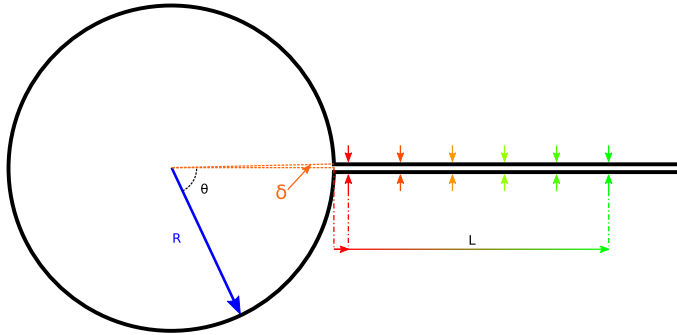


Figure 2.2: **Cross-section of the experimental system.** The dendritic spine head was mimicked by a giant unilamellar vesicle of radius  $R$ . The spine neck was simulated by a membrane nanotube of radius  $r$ . Lipid-anchored quantum dots served as surrogate of membrane receptors. Receptor escape was monitored by observation of quantum-dots that crossed a virtual finish-line at distance  $L_0 = 2 \mu\text{m}$  (red arrows) up to  $L = 10 \mu\text{m}$  (other arrows) into the tube.

Lastly, receptor proteins were imitated by lipids which were labeled by individual fluorescent quantum-dots. Trajectories of individual lipid-anchored quantum dots undergoing diffusion on the membrane were followed at high spatial (20 nm) and temporal (30 ms) resolution on a wide-field single-molecule microscope (figure 2.3). For comparison of results obtained in our biomimetic system with those *in vivo*, the higher mobility of lipids with respect to transmembrane receptors had to be considered. Given the about hundred-fold higher

values of the diffusion constants for the mimetic with respect to the *in vivo* situation ( $0.5 \mu\text{m}^2/\text{s}$  vs.  $0.01 \mu\text{m}^2/\text{s}$  [22]), in combination with the about ten times larger size  $R$  of the mimetic versus the *in vivo* systems ( $2 - 50 \mu\text{m}$  vs.  $0.1 - 1 \mu\text{m}$  [23]), we predicted that the timescales we found are about similar in the *in vivo* systems given the scaling of diffusion processes  $R^2/D$ .

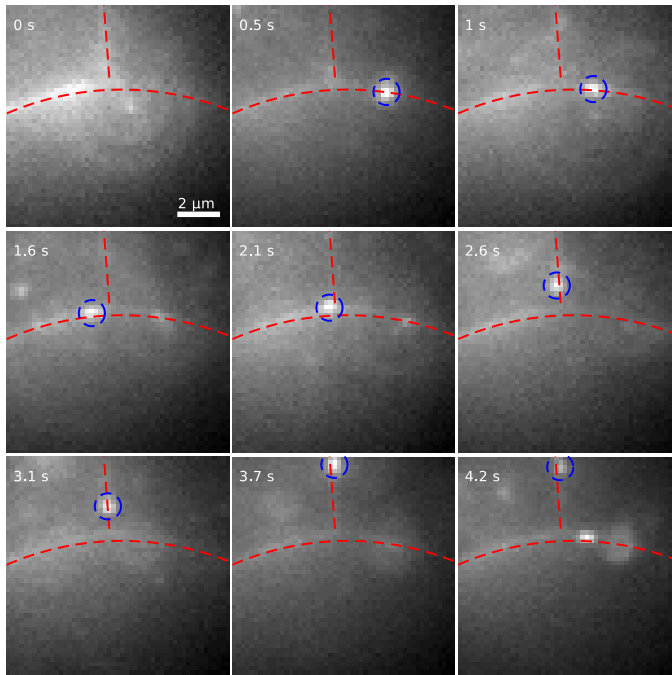


Figure 2.3: **Example of an escape event in an artificial dendritic spine.** A quantum dot mimicking a receptor in a GUV/tube system (marked by the red line) was followed in time. Initially, the quantum dot (bright signal) was outside the depth of focus. At  $t = 0.5 \text{ s}$ , it appeared in focus (marked by the blue circle) on the membrane of the GUV. After about  $2.5 \text{ s}$  it entered the tube in which it diffused further. After about  $3.5 \text{ s}$  it is passed the finish line at  $L_0 = 2 \mu\text{m}$  and was counted as escaped.

### 2.2.2 Diffusion constant

We were interested in the rate at which receptors, i.e. lipid-anchored quantum-dots, escaped the dendritic spine. Therefore we used single-molecule microscopy to follow individual lipid-anchored quantum dots on the membrane in the vesicle/tube mimetic. Individual quantum dots were followed at high spatial (20 nm) and temporal (30 ms) resolution for an extensive time-scale (up to 10 s) in an axial slice of  $\sim 1 \mu\text{m}$  thickness through the GUV. The imaging plane contained the plane of the membrane tube (figure 2.3). A selection of typical trajectories is shown in figure 2.4. The observed trajectories were split into several modes which encompass all our observations: (i) quantum dots which diffused on the membrane of the GUV within our observation slice, (ii) quantum dots that diffused on the membrane of the GUV and left the observation slice in axial direction, (iii) quantum dots that diffused up and down the membrane tube, (iv) quantum dots that diffused out of the GUV into the tube or *vice versa*. The latter were the events that we further analyzed in terms of the escape problem.

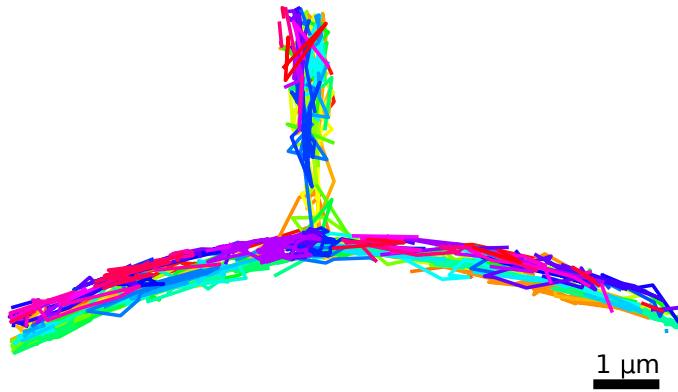


Figure 2.4: **Selection of trajectories of quantum dots on the surface of an artificial dendritic spine.** The selection includes the trajectory of the quantum dot tracked in figure 2.3. Colors denote different trajectories.

An example of a quantum dot (encircled in blue) that escaped the artificial spine (outlined in red) is shown in figure 2.3. The sequence was recorded at 9.5 Hz, such that the imaging kept up with the movement of the quantum dot. Initially, the quantum dot was not visible. At  $t = 0.5$  s, the quantum dot appeared in the image plane of the GUV (bottom) that contained the long membrane tube (top). After 2.5 s the quantum dot entered the tube. 1 s later it passed the virtual finish line we defined at  $L_0 = 2 \mu\text{m}$  into the tube and was counted as having escaped the system.  $L_0$  was chosen such that its location on the tube was clearly separated from the membrane of the giant vesicle.

The sole parameter that controls the relation between displacement and time-scale in the problem is the diffusion constant,  $D$ .  $D$  was determined from the diffusional trajectories in modes (i) and (iii) by fitting the one-dimensional mean squared displacement along the membrane as a function of the time-lag between two observations for each vesicle. The diffusion constant had an average value of  $D = (0.5 \pm 0.1) \mu\text{m}^2/\text{s}$ , (figures 2.8 and 2.9). This value coincides with diffusion constants of bead- and quantum-dot labelled lipids [24], yet are smaller than that for fluorophore-labeled lipids reported to be  $1 - 4 \mu\text{m}^2/\text{s}$  [25]. Next to the diffusion constant, analysis of trajectories in mode (iii) permitted to experimentally determine the sub-diffraction sized radius of the tube,  $r$  [26]. Trajectories were first split into movements parallel and perpendicular to the tube-direction before the respective mean-squared displacements  $\text{MSD}_{\parallel}$  and  $\text{MSD}_{\perp}$  were determined. Subsequently the time-dependence of the MSDs was determined. Where  $\text{MSD}_{\parallel}(t)$  increased linearly in time as  $\text{MSD}_{\parallel}(t) = 2Dt$ , the perpendicular component saturated for long timescales to  $\text{MSD}_{\perp}(t \rightarrow \infty) = r^2$  [26]. From the latter value the tube radius was determined. The tube radii were in the range  $r = 150 \text{ nm}$  to  $300 \text{ nm}$  (figure 2.10).

### 2.2.3 Escape rate

The methodology described in the previous subsection permitted us to directly determine the time of escape from the GUV for each quantum dot directly. However, statistics in such an approach was low given that our imaging approach required that the quantum dots stayed within the depth of focus during the entire experiment. Yet most of the trajectories we observed fall into mode (ii), where quantum dots moved out of the observation volume in the axial direction. Therefore the escape rate was determined statistically. We counted the number of quantum dots  $n$  that passed a virtual finish-line at position  $L$  in the tube within the time-period of observation  $\Delta t$ . The latter was set to 100 s yielding sufficient events  $n$  in each experiment. Subsequently, the escape rate  $E$  was determined by normalization of  $n$  by the total number of particles  $N$  on each

GUV:

$$E = \frac{n}{N\Delta t} \quad (2.1)$$

$N$  was determined experimentally for each GUV by counting the total number of particles visible in the plane of focus and taking into account the depth of focus of our microscope (see the M&M subsection).

The escape rate is a Kramers' rate, which is related to the mean first passage time  $\tau$  (MFPT) by [27]

$$\frac{1}{E} = \tau \quad (2.2)$$

It is worth noting that the escape rate is only dependent on the geometry of the artificial dendritic spine and the diffusion constant, given that  $ER^2/D$  is a unitless quantity. Thus we expected that the escape rate would scale as  $R^{-2}$ , the inverse of the surface area of the GUV.

## 2.2.4 Dependence of escape rate on GUV radius

We analyzed the escape rate for a range of GUV-tube systems. In order to reduce broadening of the data due to differences in the diffusion constants for different vesicles (see figure 2.8), escape rates  $E$  were normalized by  $D$ . The results for the ratio  $E/D$  are shown in figure 2.5 where the radius  $R$  of the GUV was varied between 4 - 20  $\mu\text{m}$ . Data are shown in blue and include standard errors represented by blue bars. The range of values of  $10^{-5}$  -  $10^{-3}/\mu\text{m}^2$  found for  $E/D$  translates into mean-first-passage times between 8 min and 1 day, taking into account the diffusion constant of  $D = 0.5 \mu\text{m}^2/\text{s}$  reported above. A fit to a power-law  $E/D = \Gamma R^{-\alpha}$  (red line) revealed that the escape rate scaled with an exponent  $\alpha = 2.6 \pm 0.3$  of the vesicle radius. Hence the dependence was stronger than the quadratic dependence predicted from scaling with the surface area of the GUV. The mobility factor was determined to  $\Gamma = (0.27 \pm 0.18) \mu\text{m}^{\alpha-2}$ .

As noted earlier, the system under study is an example of the narrow-escape problem. An analytical solution for the MFPT of the narrow-escape problem has been derived for particles diffusing on a spherical shell attached to a cylindrical tube [28]. The solution for an arbitrary starting point on the GUV, as defined by the polar angle  $\theta$  with respect to the plane of the membrane tube is given by [28]:

$$E(\theta, R, L) = D \left[ 2R^2 \log \left( \frac{\sin \theta/2}{\sin \delta/2} \right) + \frac{L^2}{2} + \frac{2R^2 L}{r} \right]^{-1} \quad (2.3)$$

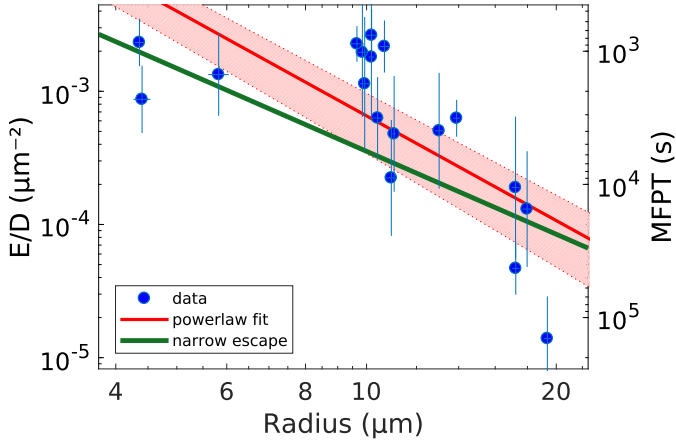


Figure 2.5: **Ratio of escape rate and diffusion constant ( $E/D$ ) for changing GUV-radius.** Data-points and standard errors are shown in blue. The red line follows a power-law fit to the data yielding an exponent of  $-2.6 \pm 0.3$ . The prediction interval for this fit is shown as red-shaded region. The green line displays the full theoretical prediction for a vesicle/tube geometry [28], with tube-radius  $r = 200$  nm, and tube-length  $L_0 = 2$   $\mu\text{m}$

The opening of the attached membrane tube  $\delta = \arcsin(r/R)$  defines the minimum possible angle in  $\theta$ . Integration of equation (2.3) with respect to all starting positions on the sphere leads to an expression for the total escape rate as measured in our experiments (see supplementary section 2.6.1):

$$\frac{E(R, L)}{2Dr^{-2}} = \left[ \frac{4R^2}{r^2} \left( \frac{\log\left(\frac{2}{1-\sqrt{1-r^2/R^2}}\right)}{1+\sqrt{1-r^2/R^2}} + \frac{L}{r} - 1 \right) + \frac{L^2}{r^2} \right]^{-1} \quad (2.4)$$

The result of equation (2.4) for a mean tube radius  $r = 200$  nm and  $L = L_0 = 2$   $\mu\text{m}$  was added to figure 2.5 (green line). The analytical curve follows the experimental data within experimental uncertainty. It should be stressed that the analytical curve does not contain any free parameter.

### 2.2.5 Dependence of the escape rate on tube length

Besides the size of the head  $R$ , a second shape parameter determining the escape rate is the length of the tube  $L$ . In contrast to the GUV radius,  $L$  was modified by repositioning the virtual finish-line on the tube. Whereas, in the experiments referred to in the last subsection we kept  $L = L_0 = 2 \mu\text{m}$  constant, here  $L$  was varied between 2 and 6  $\mu\text{m}$ .

In order to retrieve the scaling behavior of the escape rate on  $L$ , we rescaled all results by the power-law dependence  $R^{-\alpha}$ ,  $\alpha = 2.6$ , that we experimentally determined in the last subsection. After this rescaling, all data fall onto a single master curve (figure 2.5), which allowed us to analyze all experiments globally, and independent of  $R$ . It should be noted, that the rescaled data also includes the linear term  $L/r$  in equation (2.4) which accounts for molecules that returned into the GUV before crossing the finish line defined by  $L$  [28]. The inverse of the rescaled ratio of escape-rate to diffusion constant is well approximated by a second-order polynomial in  $L$ , reading

$$\left[ \frac{E(R, L)}{D \Gamma R^{-\alpha}} \right]^{-1} = 1 + p (L - L_0)^2 \quad (2.5)$$

As predicted for diffusion, the inverse escape-rate increases quadratically with the tube length. All data closely followed the behavior predicted from equation (2.5) (figure 2.6). Each data point (blue line) in figure 2.6 is the average scaled inverse escape-rate  $D \Gamma R^{-\alpha} / E$  at a given position  $L$  on the tube. The red line represents a free fit of the data to equation (2.5), yielding values for the parameter  $p = (1.84 \pm 0.03) / \mu\text{m}^2$ .

## 2.3 Discussion & Conclusion

The system described here is a very simplified model for a real dendritic spine, yet it is complex enough to display some of the essential ingredients. Our data demonstrate the dependence of the escape rate on morphology. The escape-rate from the head of a dendritic spine into the tube decreases about a hundred-fold when the size of the head is increased five-fold. This shows that the dependence exceeds the scaling that would be predicted solely by the quadratic increase in surface area. In addition, increasing the length of the tube that connects the head of the dendritic spine to the axon, decreases the escape rate further. The quadratic dependence of the escape rate  $E$  on the length of the tube  $L$  is recovered from our data. Increasing the length of the tube  $L$  three-fold decreases the escape rate thirty-fold.

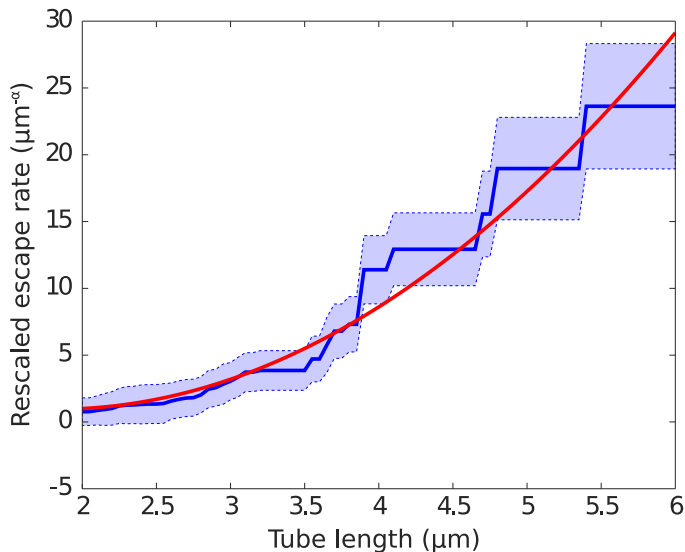


Figure 2.6: **Escape-rate versus tube length.** Inverse of the ratio of the rescaled escape-rate to the diffusion constant with increasing tube length.

A quantitative comparison between the influence of the neck- *vs.* the head-region is given in figure 2.7. From the figure it becomes apparent that the size of the head is dominant with respect to retention of receptors out of the spine. The dashed lines represent geometries for which the mean first-passage time is 1 s, 1 min, 1 h, and 12 h, respectively. The timescales we determined for lipid escape on the model system of 8 min - 1 day are about one order of magnitude longer than we would predict in the spine, since the model system is larger than typical structures observed *in vivo* by about two orders of magnitude, and the diffusion constant in the mimetic system ( $D = 0.5 \mu\text{m}^2/\text{s}$ ) is about one order of magnitude higher than the receptor diffusion constant reported in the spine ( $D = 0.02 \mu\text{m}^2/\text{s}$ , [15]).

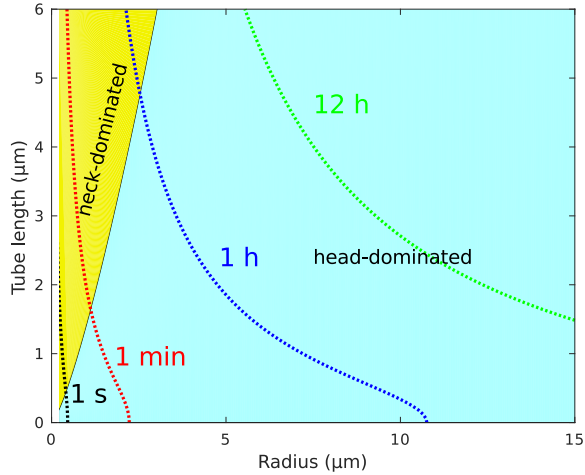


Figure 2.7: **A quantitative comparison between the influence of the neck- vs. the head-region.** is given in figure 2.7. The blue region indicates the morphology of the system where the radius of the head is the dominant determiner for the retention of receptors. The yellow region indicates the morphology of the system where the radius of the neck is the dominant determiner for the retention of receptors. The dashed lines represent geometries for which the mean first-passage time is 1 s (black), 1 min (red), 1 h (blue), and 12 h (green), respectively.

Although our analysis clearly shows the influence of spine morphology on the escape rate, the retention times up to a few hours in our mimetic system, which translates to minutes in a real dendritic spine, would be clearly insufficient for the long-term memory capability of our brain. It is obvious that our simple mimetic system lacks the large number of proteins which cells have, some of which are known to inhibit diffusion on the spine membrane and through the spine neck [7, 15, 29]. Hence, certainly for memory and learning these mechanisms together with active transport of receptors towards the synapse will be the main determinants.

Yet, the reduction of the escape rate due to morphology may play a role in the initial formation of neuronal connections, leaving sufficient time that other structural rearrangements like those mentioned above can be built up. It is known that developing dendritic spines start out as a protrusion, without a restricting neck region, reducing passage times to probably far under a second. In these young spines, therefore, it is very easy to adapt the number of receptors as is required for learning. Conversely, the restricting behavior of specialized proteins and active transport of new receptors into the dendritic spine, aided by the minutes-long passage times in dendritic spines with large heads and long necks, achieve a life-long memory or long-term potentiation (LTP).

## 2.4 Acknowledgements

This work is part of the research programme "Barriers in the Brain", granted by of the Foundation for Fundamental Research on Matter (FOM), which is part of the Netherlands Organisation for Scientific Research (NWO).

## 2.5 Materials and Methods

### 2.5.1 GUV preparation

Giant unilamellar vesicles (GUVs) were prepared using electroswelling [20]. 20  $\mu$ l lipids (1,2-dioleoyl-*sn*-glycero-3-phosphocholine (Avanti Polar Lipids 850375C, DOPC) and 1,2-dioleoyl-*sn*-glycero-3-phosphoethanolamine-N-(biotinyl) (Avanti Polar Lipids 870282C, bioDOPE)) dissolved in chloroform (2 g/L) were deposited on top of two indium tin oxide (ITO) coated glasses (total covered area about 10 cm<sup>2</sup>). The chloroform was evaporated for two hours using a desiccator. Subsequently the coated glasses were placed parallel, coated sides facing each other in a teflon enclosure with about 3 mm separation between them. The space between the glasses was filled with 230 mOsmol/kg sucrose. Swelling was done for two hours at 10 Hz, 4 V<sub>pp</sub> sinusoidal excitation. After that the sucrose solution containing the GUVs was extracted from the chamber.

### 2.5.2 Receptor mimicry

Quantum dots (Qdot705 Streptavidin Conjugate; Q10163MP, Life Technologies) were gently mixed with GUVs after electroswellling. Then GUVs were diluted  $40\times$  in 300 mOsmol/kg phosphate buffered saline (PBS). The streptavidin-coated quantum dots bound to the biotinylated lipids of the GUV membranes (about 1% bioDOPE. The microscope coverglass was treated with 1 mL, 1 g/L BSA-biotin (Sigma) and 1 mL, 60  $\mu\text{g/L}$  neutravidin (Sigma), for fifteen minutes each, and washed with PBS after and in between, to enable the GUVs to bind to the glass.

A membrane nanotube was pulled out of the GUV with a micromanipulator (Narishige MW3) equipped with a glass microneedle (Harvard glass) pulled into a tip with an opening less than 1  $\mu\text{m}$  in diameter (Sutter Puller P90). GUVs were gently punched with the needle until the membrane was stuck to the needle. Subsequently, the needle was retracted and a membrane nanotube was formed.

### 2.5.3 Imaging

Imaging was performed on an epi-fluorescence microscope. Illumination was performed using a 488 nm, 100 mW laser (Coherent Sapphire 488-100 CW CDRH). The laser beam was modulated by an acousto-optical tunable filter (AA-OptoElectronic, AOTFnC-VIS) to illuminate the sample only when the camera was in exposure mode. Via a tube-lens, the laser beam was coupled into a Zeiss Axiovert 100 microscope fitted with a Zeiss  $100\times$  NA 1.4 oil immersion objective resulting in Köhler illumination of the sample. The excitation and emission paths were split using a dichroic mirror (Semrock Di01-R405/488/561/635) and an emission filter (Chroma ZET405/488/561/640m). Detection was done using a CCD camera (Roper Scientific/Princeton Instruments 1340B combined with an ST133 controller and WinView32 software), cooled to  $-90^\circ\text{C}$  using liquid nitrogen.

### 2.5.4 Particle tracking

Images were analyzed using home-made Matlab software as described before [30]. Briefly, because the size of a single quantum dot was in the range of 10 nm, the photons emitted were spread on the pixels of the CCD sensor by the point spread function of the microscope. These signals were fit to two-dimensional Gaussians, resembling the point-spread function. In this way,

we were able to determine the center-of-mass position of the quantum dots with up to 20 nm-precision. Tracking the quantum dots was done as described earlier [31], by calculating the probability that a particle in frame  $n$  is the same particle in frame  $n + 1$  and maximizing this probability with respect to other connectivities.

### 2.5.5 Escape rate

After obtaining the tracks, the number of particles that escaped the system per unit of time was counted. In most experiments a particle was counted when it crossed a virtual plane perpendicular to the tube at  $L = L_0 = 2 \mu\text{m}$  from the edge of the GUV (figure 2.2). In other experiments the distance  $L$  was varied. This number was subsequently normalized to the total number of particles  $N$  on the GUV. In this way the escape rate  $E$  was calculated:

$$E = f \frac{n}{N} = f \frac{n}{n_{\text{vis}}} \frac{lz}{4\pi R^2} \quad (2.6)$$

Here  $n$  is the total number of particles that escaped during the whole experiment.  $f = 9.5 \text{ Hz}$  is the frame-rate of the camera. The total number of particles  $N$  on the GUV was estimated using the visible number of particles in all frames and the fraction of the GUV surface area that is visible in the field of view  $lz/A$ , with  $l$  the length of the contour in the field of view,  $z$  the depth of focus, and  $4\pi R^2$  the surface area of the GUV. In this definition the escape rate  $E$  is a Kramers' rate. Therefore the escape rate  $E$  is related to the mean first passage time  $\tau$  (MFPT) frequently referred to in literature [32]:

$$\tau = \frac{1}{E} \quad (2.7)$$

## 2.6 Supplementary information

### 2.6.1 Angular average of the escape rate

The equation for the escape rate equation (2.3) in general contains a term that describes escape from the head to the tube, and a term for escape from the tube. Here we will focus just on the first:

$$\begin{aligned} \tau_{\text{head}}(\theta) &= \frac{2R^2}{D} \log \left( \frac{\sin \theta/2}{\sin \delta/2} \right) \\ &= \frac{2R^2}{D} (\log(\sin \theta/2) - \log(\sin \delta/2)) \end{aligned} \quad (2.8)$$

The earlier escape rate contains the starting position of the diffusing object in terms of its azimuthal angle  $\theta$  with respect to the line defined by the membrane tube. To obtain an average escape rate equation (2.8) must be averaged for all angles:

$$\begin{aligned} \langle \tau_{\text{head}} \rangle_{\theta} &= \frac{\int_0^{2\pi} \int_{\delta}^{\pi} \tau_{\text{head}}(\theta) R^2 \sin \theta \, d\theta \, d\phi}{\int_0^{2\pi} \int_{\delta}^{\pi} R^2 \sin \theta \, d\theta \, d\phi} \\ &= \frac{\int_{\delta}^{\pi} \tau_{\text{head}}(\theta) \sin \theta \, d\theta}{\int_{\delta}^{\pi} \sin \theta \, d\theta} \end{aligned} \quad (2.9)$$

Using the definitions

$$\begin{aligned} A &= \cos \delta = \sqrt{1 - r^2/R^2} \\ B &= \cos \theta ; \sin \theta \, d\theta = -dB \end{aligned} \quad (2.10)$$

Equation (2.9) becomes

$$\begin{aligned} \langle \tau_{\text{head}} \rangle_{\theta} &= \frac{\int_{-1}^A \tau_{\text{head}}(\theta) \, dB}{\int_{-1}^A \, dB} \\ &= \frac{R^2}{D(1+A)} \int_{-1}^A \log\left(\frac{1-B}{2}\right) - \log\left(\frac{1-A}{2}\right) \, dB \\ &= \frac{R^2}{D(1+A)} \left( \int_{-1}^A \log\left(\frac{1-B}{2}\right) \, dB - \int_{-1}^A \, dB \log\left(\frac{1-A}{2}\right) \right) \end{aligned} \quad (2.11)$$

Integration yields,

$$\begin{aligned} \langle \tau_{\text{head}} \rangle_{\theta} &= \frac{R^2}{D(1+A)} \left( \left[ (B-1) \log\left(\frac{1-B}{2}\right) - B \right]_{B=-1}^A - (1+A) \log\left(\frac{1-A}{2}\right) \right) \\ &= \frac{R^2}{D(1+A)} \left( (A-1) \log\left(\frac{1-A}{2}\right) - A - 1 - (1+A) \log\left(\frac{1-A}{2}\right) \right) \\ &= \frac{R^2}{D} \left( \frac{2 \log\left(\frac{2}{1-A}\right)}{1+A} - 1 \right) \end{aligned} \quad (2.12)$$

which finally leads to the expression used in equation (2.3) for the angle-averaged escape rate from a spherical object of Radius  $R$  into a tube of radius  $r$

## 2.6.2 Diffusion constants

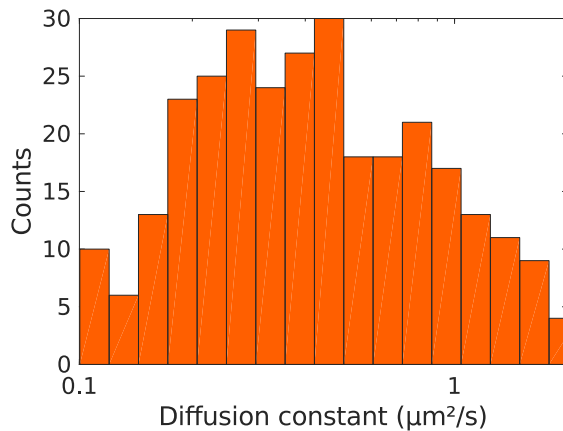


Figure 2.8: **Diffusion constant distribution on the GUv from 320 trajectories.** The average diffusion constant was  $D_{GUv} = (0.5 \pm 0.4) \mu\text{m}^2/\text{s}$ .

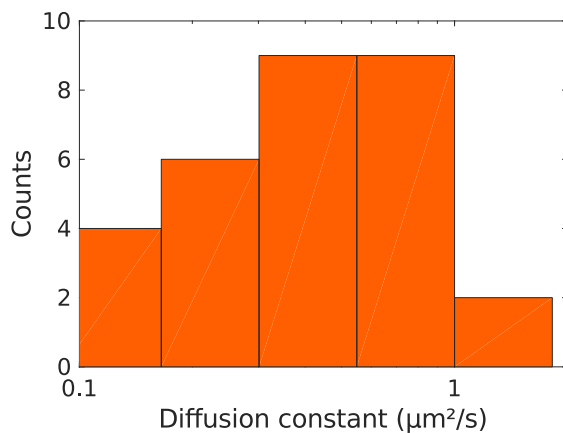


Figure 2.9: **Diffusion constant distribution on the tube from 34 trajectories.** The average diffusion constant was  $D_{\text{tube}} = (0.4 \pm 0.3) \mu\text{m}^2/\text{s}$ .

### 2.6.3 Tube Radius

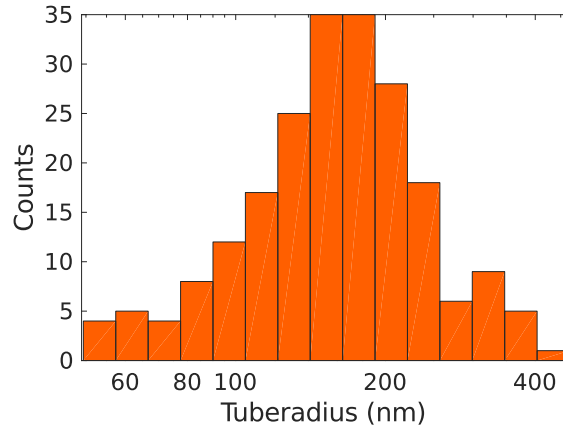


Figure 2.10: Radii of 22 tubes estimated from the perpendicular diffusion of 212 quantum dots. The average radius was  $r = (200 \pm 50)$  nm.

## References

- [1] H. Hering and M. Sheng. “Dendritic spine: structure, dynamics and regulation”. In: *Nat. Rev. Neurosci.* 2.12 (2001), pp. 880–888. DOI: 10.1038/35104061.
- [2] D. Axelrod et al. “Lateral motion of fluorescently labeled acetylcholine receptors in membranes of developing muscle fibers”. In: *Proc. Natl. Acad. Sci.* 73.12 (1976), pp. 4594–4598. DOI: 10.1073/pnas.73.12.4594.
- [3] A. Sergé et al. “Receptor activation and homer differentially control the lateral mobility of metabotropic glutamate receptor 5 in the neuronal membrane”. In: *J. Neurosci.* 22.10 (2002), pp. 3910–3920.
- [4] J. Meier et al. “Formation of glycine receptor clusters and their accumulation at synapses”. In: *J. Cell Sci.* 113 (2000), pp. 2783–2795.
- [5] A. J. Borgdorff and D. Choquet. “Regulation of AMPA receptor lateral movements”. In: *Nature* 417.6889 (2002), pp. 649–653. DOI: 10.1038/nature00780.
- [6] J. Meier et al. “Fast and reversible trapping of surface glycine receptors by gephyrin”. In: *Nat. Neurosci.* 4.3 (2001), pp. 253–260. DOI: 10.1038/85099.
- [7] D. Choquet and A. Triller. “The role of receptor diffusion in the organization of the postsynaptic membrane”. In: *Nat. Rev. Neurosci.* 4.4 (2003), pp. 251–265. DOI: 10.1038/nrn1077.
- [8] T. Schikorski and C. F. Stevens. “Quantitative fine-structural analysis of olfactory cortical synapses”. In: *Proc. Natl. Acad. Sci.* 96.7 (1999), pp. 4107–4112. DOI: 10.1073/pnas.96.7.4107.
- [9] J. I. Arellano. “Ultrastructure of dendritic spines: correlation between synaptic and spine morphologies”. In: *Front. Neurosci.* 1.1 (2007), pp. 131–143. DOI: 10.3389/neuro.01.1.1.010.2007.
- [10] J. N. Bourne and K. M. Harris. “Balancing structure and function at hippocampal dendritic spines”. In: *Annu. Rev. Neurosci.* 31.1 (2008), pp. 47–67. DOI: 10.1146/annurev.neuro.31.060407.125646.
- [11] P. Hotulainen and C. C. Hoogenraad. “Actin in dendritic spines: connecting dynamics to function”. In: *J. Cell Biol.* 189.4 (2010), pp. 619–629. DOI: 10.1083/jcb.201003008.

- [12] M. Frotscher et al. “Fine structure of synapses on dendritic spines”. In: *Front. Neuroanat.* 8.September (2014), pp. 1–9. DOI: 10.3389/fnana.2014.00094.
- [13] M. Adrian et al. “Probing the interplay between dendritic spine morphology and membrane-bound diffusion”. In: *Biophys. J.* 113 (2017), pp. 1–10. DOI: 10.1016/j.bpj.2017.06.048.
- [14] A. Attardo, J. E. Fitzgerald, and M. J. Schnitzer. “Impermanence of dendritic spines in live adult CA1 hippocampus”. In: *Nature* 523 (2015), pp. 592–596. DOI: 10.1038/nature14467.
- [15] H. Ewers et al. “A septin-dependent diffusion barrier at dendritic spine necks”. In: *PLoS One* 9.12 (2014), e113916. DOI: 10.1371/journal.pone.0113916.
- [16] D. Holcman and Z. Schuss. “The narrow escape problem”. In: *SIAM Rev.* 56.2 (2014), pp. 213–257. DOI: 10.1137/120898395.
- [17] R. Kusters et al. “Shape-induced asymmetric diffusion in dendritic spines allows efficient synaptic AMPA receptor trapping”. In: *Biophys. J.* 105.12 (2013), pp. 2743–2750. DOI: 10.1016/j.bpj.2013.11.016.
- [18] M. Adrian et al. “Barriers in the brain: resolving dendritic spine morphology and compartmentalization”. In: *Front. Neuroanat.* 8.12 (2014), pp. 1–12. DOI: 10.3389/fnana.2014.00142.
- [19] G. Adam and M. Delbrück. “Reduction of dimensionality in biological diffusive processes”. In: *Struct. Chem. Mol. Biol.* 1968, pp. 198–215.
- [20] M. I. Angelova and D. S. Dimitrov. “Liposome electroformation”. In: *Faraday Discuss. Chem. Soc.* 81 (1986), pp. 303–311. DOI: 10.1039/dc9868100303.
- [21] I. Derényi, F. Jülicher, and J. Prost. “Formation and interaction of membrane tubes”. In: *Phys. Rev. Lett.* 88.23 (2002), pp. 1–4. DOI: 10.1103/PhysRevLett.88.238101. arXiv: 0205630 [cond-mat].
- [22] M. Dahan. “Diffusion dynamics of glycine receptors revealed by single-quantum dot tracking”. In: *Science* 302.5644 (2003), pp. 442–445. DOI: 10.1126/science.1088525.
- [23] J. N. Bourne and K. M. Harris. “Nanoscale analysis of structural synaptic plasticity”. In: *Curr. Opin. Neurobiol.* 22.3 (2012), pp. 372–382. DOI: 10.1016/j.conb.2011.10.019.
- [24] M. J. Murcia et al. “Design of quantum dot-conjugated lipids for long-term, high-speed tracking experiments on cell surfaces”. In: *J. Am. Chem. Soc.* 130.45 (2008), pp. 15054–15062. DOI: 10.1021/ja803325b.

- [25] A. Sonnleitner, G. J. Schütz, and T. Schmidt. “Free Brownian motion of individual lipid molecules in biomembranes”. In: *Biophys. J.* 77.November (1999), pp. 2638–2642. DOI: 10.1016/S0006-3495(99)77097-9.
- [26] S. Wieser et al. “Single molecule diffusion analysis on cellular nanotubules: Implications on plasma membrane structure below the diffraction limit”. In: *Appl. Phys. Lett.* 91.23 (2007), p. 233901. DOI: 10.1063/1.2822890.
- [27] D. Boilley, B. Jurado, and C. Schmitt. “Simple relations between mean passage times and Kramers’ stationary rate”. In: *Phys. Rev. E - Stat. Nonlinear, Soft Matter Phys.* 70.5 2 (2004), pp. 1–4. DOI: 10.1103/PhysRevE.70.056129.
- [28] D. Holcman and Z. Schuss. “Diffusion laws in dendritic spines”. In: *J. Math. Neurosci.* 1.10 (2011), pp. 1–14. DOI: 10.1186/2190-8567-1-10.
- [29] B. Winckler et al. “A diffusion barrier maintains distribution of membrane proteins in polarized neurons”. In: *Nature* 397.2 (1999), pp. 698–701. DOI: 10.1038/17806.
- [30] T. Schmidt et al. “Imaging of single molecule diffusion”. In: *Proc. Natl. Acad. Sci. USA* 93.7 (1996), pp. 2926–2929. DOI: 10.1073/pnas.93.7.2926.
- [31] G. J. Schütz, H. Schindler, and T. Schmidt. “Single-molecule microscopy on model membranes reveals anomalous diffusion”. In: *Biophys. J.* 73.2 (1997), pp. 1073–1080. DOI: 10.1016/S0006-3495(97)78139-6.
- [32] P. Reimann, G. J. Schmid, and P. Hänggi. “Universal equivalence of mean first-passage time and Kramers rate”. In: *Phys. Rev. E. Stat. Phys. Plasmas. Fluids. Relat. Interdiscip. Topics* 60.1 (1999), R1–R4. DOI: 10.1103/PhysRevE.60.R1.

